



Cite this: DOI: 10.1039/c5dt01157d

Anion coordination selective [Mn₃] and [Mn₄] assemblies: synthesis, structural diversity, magnetic properties and catechol oxidase activity†‡

Moumita Pait,^a Michael Shatruk^b and Debashis Ray*^a

Syntheses, crystal structures, magnetic properties and catechol oxidation behavior are presented for [Mn₃] and [Mn₄] aggregates, [Mn^{II}₂Mn^{III}(O₂CMe)₄(dmp)₂(H₂O)₂]·2H₂O (**1**·2H₂O), [Mn^{II}₂Mn^{III}(O₂CCH₂Cl)₄(dmp)₂(H₂O)₂]·H₂O·MeOH (**2**·H₂O·MeOH), [Mn^{II}₄(μ₃-O)(dmp)₄(μ-DMSO)(N₃)(DMSO)(H₂O)]ClO₄·DMSO (**3**·ClO₄·DMSO), and [Mn^{II}₄(μ₃-O)(dmp)₄(μ-DMSO)(ClO₄)(DMSO)(H₂O)]ClO₄·DMSO (**4**·ClO₄·DMSO), developed with single type ligand H₂dmp, 2-[(2-hydroxy-1,1-dimethyl-ethylimino)-methyl]-phenol. The successful isolation of **1–4** resulted from a systematic exploration of the effect of Mn^{II} salts, added carboxylates, Mn/H₂dmp ratio, presence of azide, and other reaction conditions. The cores of **1** and **2** are similar and consist of a linear Mn^{II}Mn^{III}Mn^{III} unit in a carboxylate and H₂dmp environment, revealing a central Mn^{II} ion in a different environment and terminal Mn^{III} ions available for the introduction of structural and magnetic anisotropy to the system. The cores of **3** and **4** are also similar and consist of a distorted incomplete-adamantane type Mn₄ coordination assembly in a carboxylate-free environment built on a triangular [Mn^{III}(μ₃-O)] unit. The magnetic behavior of complexes **1–3** is dominated by antiferromagnetic exchange coupling that results in ground state spin values of *S* = 3/2 for **1** and **2** and *S* = 0 for **3**. In solution, all four complexes **1–4** show catechol oxidation activity towards 3,5-DTBC. The catalytic activity for the oxidation of 3,5-DTBC in air followed the order **4** < **3** < **1** < **2**.

Received 24th March 2015,
Accepted 12th May 2015

DOI: 10.1039/c5dt01157d

www.rsc.org/dalton

Introduction

Multinuclear manganese complexes exhibit a variety of aesthetically pleasing structures that span a range of oxidation states (Mn^{II}, Mn^{III}, and Mn^{IV}).^{1–3} These molecular edifices continue to attract synthetic coordination chemists due to their function as enzymes mimics, magnetically coupled clusters, and oxidation catalysts.^{4,5} Four manganese centers have been identified in the oxygen-evolving center (OEC) in the photosystem II of plants and cyanobacteria.^{6–8} The synthetically controlled aggregation of manganese ions can be tuned to obtain ferromagnetically coupled clusters with large spin ground states.^{9–11} Introduction of Mn^{III} ions in such clusters provides the source of significant magnetic anisotropy and can be employed for the design and preparation of single-molecule magnets.¹² Multinuclear complexes containing several Mn

centers in close proximity have been utilized as a new generation of large-spin molecules with a promise to show SMM behavior, catalytic activity and catechol oxidation.¹³ Catechol oxidase is a copper containing type 3 active-site protein that catalyzes the oxidation of a range of *o*-diphenols (catechols) to *o*-quinones. Although catechol oxidases have copper at the active site, investigations have also been shown that some Mn(II/III/IV), Ni(II) and Co(II/III) complexes can also promote such activity.¹⁴

Thus, there continues to be a need to develop and standardize newer methodologies and synthetic strategies for the controlled assembly of multinuclear manganese complexes with interesting magnetic, physical and catalytic properties. Recently, [Mn₁₂] clusters have been scrutinized as efficient oxidation catalysts.¹⁵ In recent time, the role of the primary ligand system, nature and number of co-ligands and presence of coordinating solvents in the assembly processes has been the topic of contemporary interest. Alcohol-arm bearing tridentate ligands coordinated to a metal ion have the propensity to bind to adjacent metal ions through bridges from their alkoxido groups in the deprotonated form. Among the supporting co-ligands, carboxylate and hydroxide groups are versatile for extending the bridge structure at the vacant coordination sites around the metal ion. In trying to isolate and study new forms of such coordination clusters, we have been exploring manga-

^aDepartment of Chemistry, Indian Institute of Technology, Kharagpur 721 302, India.
E-mail: dray@chem.iitkgp.ernet.in; Fax: (+91) 3222-82252; Tel: (+91) 3222-283324

^bDepartment of Chemistry & Biochemistry, Florida State University, Tallahassee,
FL 32306, USA

† Dedicated to Prof. A. Chakravorty on the occasion of his 80th birthday

‡ Electronic supplementary information (ESI) available. CCDC 1007135–1007138.
For ESI and crystallographic data in CIF or other electronic format see DOI:
10.1039/c5dt01157d

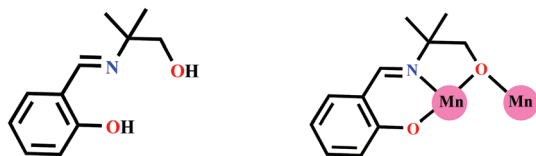


Chart 1 Ligand used in this study and its binding mode in $[\text{Mn}_3]$ and $[\text{Mn}_4]$ complexes.

nese carboxylate and hydroxide aggregates through the use of a ONO-donor tridentate chelate 2-[(2-hydroxy-1,1-dimethyl-ethylimino)-methyl]-phenol (H_2dmp) (Chart 1). This ligand was used earlier to provide $[\text{Ni}_3]$ and $[\text{Cu}_4]$ complexes as reported by Dey *et al.*¹⁶ Herein, we present two types of $[\text{Mn}_3]$ and $[\text{Mn}_4]$ complexes assembled by the coordination of ligand-bound mononuclear Mn building units *via* small ancillary groups.

Several reaction systems have been explored, involving carboxylate, azide and carbonate ions and crystallization solvent, DMSO. Carboxylate groups and water molecules function as auxiliary bridging and terminal monodenate ligands, respectively, in mixed-valent $[\text{Mn}_3]$ complexes, $[\text{Mn}_2^{\text{III}}\text{Mn}^{\text{II}}(\text{O}_2\text{CR})_4(\text{dmp})_2(\text{H}_2\text{O})_2]$ ($\text{R} = \text{Me}$, **1** and CH_2Cl , **2**). In the other two complexes, the μ_3 -oxido participates in the formation of a $[\text{Mn}_3(\mu\text{-O})]$ unit and support from the DMSO ligand resulted in adamantane-like $[\text{Mn}_4]$ complexes, $[\text{Mn}_4^{\text{III}}(\mu_3\text{-O})(\text{dmp})_4(\mu\text{-DMSO})(\text{X})(\text{DMSO})(\text{H}_2\text{O})]\text{ClO}_4$ ($\text{X} = \text{N}_3^-$, **3** and ClO_4^- , **4**) in a mixed coordination environment. All four complexes have been isolated and crystallographically characterized. Their solid state magnetic properties and solution phase catalytic activities have also been examined.

Experimental section

Materials

The solvents and chemicals used were obtained from SRL, India, Sigma-Aldrich and Loba Chemie Laboratory Reagents & Fine Chemicals, India. $\text{Mn}(\text{ClO}_4)_2 \cdot 6\text{H}_2\text{O}$ was freshly prepared by treating manganese carbonate (11.4 g, 0.1 mol) with 12.03 mL of perchloric acid (1 : 2) and crystallized after concentration on a water bath. Sodium chloroacetate was prepared by treating chloroacetic acid (14.1 g, 0.15 mol) with solid sodium hydroxide (6.0 g, 0.15 mol) followed by concentration and crystallization on a water bath. All other chemicals and solvents were reagent grade and used as received without further purification.

Caution!! Although no such behavior was observed during the present study, azides and perchlorate salts, involving organic ligands, are potentially explosive; such compounds should be synthesized and used in small quantities, and treated with utmost care at all times.

Syntheses. H_2dmp ligand

2-[(2-Hydroxy-1,1-dimethyl-ethylimino)-methyl]-phenol used in the present study was prepared from a single-step conden-

sation of salicylaldehyde (1.0 mL, 10 mmol) with 2-amino-2-methyl-1-propanol (0.952 g, 10 mmol) in MeOH (25 mL) under reflux for 1 h. The product was obtained as a yellow solid by triturating with hexane and further recrystallized from MeOH as reported earlier.¹⁶

$[\text{Mn}_2^{\text{III}}\text{Mn}^{\text{II}}(\text{O}_2\text{CMe})_4(\text{dmp})_2(\text{H}_2\text{O})_2] \cdot 2\text{H}_2\text{O}$ (**1**· $2\text{H}_2\text{O}$). To a stirred yellow MeOH solution (10 mL) of H_2dmp (0.19 g, 1.0 mmol), a MeOH solution (10 mL) of $\text{Mn}(\text{ClO}_4)_2 \cdot 6\text{H}_2\text{O}$ (0.54 g, 1.5 mmol) was added slowly followed by dropwise addition of NEt_3 (0.27 mL, 2.0 mmol) with stirring at room temperature in air. The orange solution formed initially changed to brown after complete addition of NEt_3 . The resulting brown solution was stirred for *ca.* 15 min, and a solution of NaOAc (2 mL, 0.16 g, 2.0 mmol) was added dropwise to the mixture. The solution immediately turned reddish brown and was stirred for another 2 h. The brown solution formed was then filtered and the filtrate was layered with an equal volume of CH_2Cl_2 . Brown single crystals of **1**· $2\text{H}_2\text{O}$ suitable for X-ray diffraction were obtained after 7 days. The yield of the crystalline compound based on total Mn was 0.294 g (66%). Anal. Calc. for $\text{C}_{30}\text{H}_{50}\text{Mn}_3\text{N}_2\text{O}_{18}$ (891.54 g mol⁻¹): C, 40.42; H, 5.65; Mn, N, 3.14. Found: C, 40.05; H, 5.89; N, 3.08. Molar conductance, Λ_{M} (MeOH solution): 28.5 S m² mol⁻¹. Selected FT-IR bands: (KBr, cm⁻¹) 3369 (br), 1588 (vs) and 1411 (vs). UV-vis spectra [λ_{max} , nm (ϵ , M⁻¹ cm⁻¹): (MeCN solution) 382 (5150), 233 (42 625).

Alternative method for the preparation of **1**

To a yellow MeOH solution (10 mL) of H_2dmp (0.19 g, 1.0 mmol), a MeOH solution (10 mL) of $\text{Mn}(\text{OAc})_2 \cdot 4\text{H}_2\text{O}$ (0.18 g, 1.5 mmol) was added slowly followed by dropwise addition of NEt_3 (0.27 mL, 2.0 mmol) with stirring at room temperature in air. The stirring of the red-brown solution was continued for 2 h. The brown solution formed was then filtered and the filtrate was layered with CH_2Cl_2 . Brown single crystals suitable for X-ray diffraction were obtained after 5 days.

$[\text{Mn}_2^{\text{III}}\text{Mn}^{\text{II}}(\text{O}_2\text{CCH}_2\text{Cl})_4(\text{dmp})_2(\text{H}_2\text{O})_2] \cdot \text{H}_2\text{O} \cdot \text{MeOH}$. (**2**· $\text{H}_2\text{O} \cdot \text{MeOH}$). Compound **2** was obtained following a method similar to that described above for **1** using $\text{NaO}_2\text{CH}_2\text{Cl}$ (0.46 g, 2.0 mmol) in place of NaOAc. After about one week, brown needle shaped crystals, suitable for X-ray study, were obtained. Yield of the crystalline compound based on total Mn was 0.308 g, 59%. Anal. Calc. for $\text{C}_{32}\text{H}_{48}\text{Cl}_4\text{Mn}_3\text{N}_2\text{O}_{18}$ (1055.34 g mol⁻¹): C, 36.42; H, 4.58; N, 2.65; found: C, 36.28; H, 4.45; N, 2.51. Molar conductance, Λ_{M} (MeOH solution): 35 S m² mol⁻¹. Selected FT-IR bands (KBr, cm⁻¹): 3427 (br), 1618 (s), 1570 (m) and 1385 (m). UV-vis spectra [λ_{max} , nm (ϵ , M⁻¹ cm⁻¹): (MeCN solution): 385 (8480), 236 (48 910).

Alternative method of preparation of **2**

The same procedure was employed as described for **1**, except for the use of $\text{Mn}(\text{O}_2\text{CCH}_2\text{Cl})_2 \cdot 4\text{H}_2\text{O}$ (0.46 g, 1.5 mmol) in place of $\text{Mn}(\text{OAc})_2 \cdot 4\text{H}_2\text{O}$. Dark-brown crystals were obtained after 6 days.

[Mn^{III}(μ₃-O)(dmp)₄(μ-DMSO)(N₃)(DMSO)(H₂O)]ClO₄·DMSO (3·ClO₄·DMSO). To a stirred yellow MeOH solution (10 mL) of H₂dmp (0.19 g, 1.0 mmol), a MeOH solution (10 mL) of Mn(ClO₄)₂·6H₂O (0.36 g, 1.0 mmol) was added slowly followed by dropwise addition of NEt₃ (0.27 mL, 2.0 mmol) with stirring at room temperature in air. The orange solution formed initially changed to brown after complete addition of NEt₃. The resulting brown solution was stirred for *ca.* 15 min, and then an aqueous solution of NaN₃ (2 mL, 0.065 g, 1.0 mmol) was added dropwise to the mixture resulting in the formation of a dark brown solution after 1 h. The reaction mixture was evaporated in air to give a brown powder, which was isolated by filtration, washed with cold MeOH and dried under vacuum over P₄O₁₀. X-ray quality deep-brown crystals of **3** were obtained by the vapor diffusion of Et₂O into a DMSO solution (v/v 1 : 1) of complex over 2 months. Yield: 0.085 g, 24% (based on Mn). Anal. Calc. for C₅₀H₇₀ClMn₄N₇O₁₇S₃ (1392.52 g mol⁻¹): C, 43.13; H, 5.07; N, 7.04; found: C, 43.19; H, 5.25; N, 7.03. Molar conductance, Λ_M (MeOH solution): 102 S m² mol⁻¹. Selected FT-IR bands (KBr, cm⁻¹): 3409 (br), 2027 (s), 1616 (s), 1303 (s), 1093 (s), 1047 (m), 762 (m) and 664 (m). UV-vis spectra [λ_{max}, nm (ε, M⁻¹ cm⁻¹)] (MeCN solution): 390 (9622), 575 (1755), 256 (13 295).

[Mn^{III}(μ₃-O)(dmp)₄(μ-DMSO)(ClO₄)(DMSO)(H₂O)]ClO₄·DMSO (4·ClO₄·DMSO). Solid Na₂CO₃ (0.21 g, 2.0 mmol) was added to a stirred MeOH solution (10 mL) of the ligand (0.19 g, 1.0 mmol) and stirring was continued for 2 h. To this yellow solution, a MeOH solution (10 mL) of Mn(ClO₄)₂·6H₂O (0.36 g, 1.0 mmol) was added and the mixture was stirred for 1 h to afford a dark brown solution. The solution was evaporated in air to give a brown powder, which was isolated by filtration, washed with cold MeOH and dried under vacuum over P₄O₁₀. The powder was dissolved in DMSO and layered with Et₂O (v/v 1 : 1). Dark-brown crystals suitable for X-ray diffraction were obtained after 15 days. The yield of the crystalline material based on total Mn was 18% (0.067 g). Anal. Calcd for C₅₀H₇₀Cl₂Mn₄N₄O₂₁S₃ (1449.94 g mol⁻¹): C, 41.42; H, 4.87; N, 3.86; found: C, 41.29; H, 4.95; N, 3.39. Molar conductance, Λ_M (MeOH solution): 113 S m² mol⁻¹. Selected FTIR bands (KBr, cm⁻¹): 3368 (br), 1670 (s), 1203(s), 1130 (s) and 1046 (m). UV-vis spectra [λ_{max}, nm (ε, L mol⁻¹ cm⁻¹)] (MeCN solution): 389 (10 608), 575 (1755), 260 nm (13 970).

Physical measurements

Elemental analyses (CHN) were performed with a Perkin-Elmer model 240C elemental analyzer. FT-IR spectra were obtained on a Perkin-Elmer 883 spectrometer. The solution electrical conductivity and electronic absorption spectra were obtained using a Unitech type U131C digital conductivity meter with a solute concentration of about 10⁻³ M and a Shimadzu UV 3100 UV-vis-NIR spectrophotometer, respectively.

Magnetic measurements were performed on microcrystalline samples of **1–4** using a Quantum Design SQUID magnetometer MPMS-XL. DC magnetic susceptibility was measured in an applied field of 0.1 T in the 1.8–300 K temperature range. Isothermal dependences of magnetization were

measured at 1.8 K with the magnetic field varying from 0 to 7 T. The data were corrected for the diamagnetic contribution from the sample holder and for the intrinsic diamagnetism of the sample using tabulated constants.¹⁷

X-ray crystallography

Suitable single crystals of **1**·H₂O, **2**·H₂O·MeOH, **3**·ClO₄·DMSO and **4**·ClO₄·DMSO were examined using a Bruker SMART APEX-II CCD diffractometer equipped with a fine focus 1.75 kW sealed tube Mo-K_α radiation (λ) 0.71073 (Å). The data were collected at 298 K, by scanning over the ω angle at a step of 0.3° and a scan speed of 5 s per frame. The SMART software was used for data acquisition. Data integration and reduction were performed with the SAINT and XPREP software.¹⁸ Multi-scan empirical absorption corrections were applied to the data using the program SADABS.¹⁹ Structures were solved by direct methods using SHELXS-97^{20a} and refined with full-matrix least squares on F² using SHELXL-97.^{20b} The locations of the heaviest atoms (Mn) were easily determined, and the O, N, and C atoms were subsequently determined from the difference Fourier maps. The non-H atoms were refined anisotropically (except the S6 and O33b of DMSO molecule). The H atoms were introduced in calculated positions and refined with fixed geometry and riding thermal parameters with respect to their carrier atoms. The high R₁/wR₂ = 0.0828/0.2539 for complex **4** is due to the presence of disordered DMSO molecules and the quality of the data set used for structure solution. Despite several attempts, we were not able to obtain better quality crystals for the compound. A summary of the crystal data and relevant refinement parameters are given in Table 1. CCDC 1007135 (**1**), 1007136 (**2**), 1007137 (**3**) and 1007138 (**4**) contain the supplementary crystallographic data for this study.

Results and discussion

Syntheses

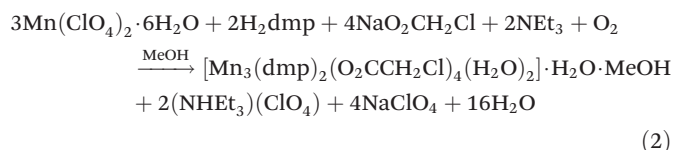
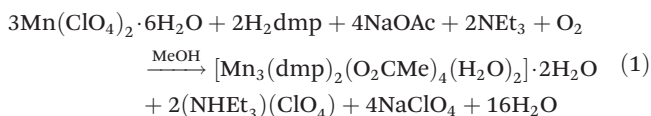
Two methods have been employed in this study to prepare [Mn₃] and [Mn₄] aggregates using a common alcohol-arm bearing ligand H₂dmp (Scheme S1, ESI†). The first one uses the reaction with Mn(ClO₄)₂ in the presence of added carboxylates and the second one employs Mn(ClO₄)₂ in the absence of any carboxylate but with sodium azide and sodium carbonate. In all the reactions, atmospheric oxygen was used for the partial or complete oxidation of Mn^{II} to Mn^{III}. Various synthetic conditions and reaction systems had been explored with other added ancillary groups before the following reproducible synthetic procedures were established. Tridentate ONO donor ligands are known to support the growth of multinuclear assemblies.²¹ The reaction of Mn(ClO₄)₂ with H₂dmp and MeCO₂Na in a 3 : 2 : 4 molar ratio in MeOH, with or without added NEt₃, led to the formation of compound **1**. The use of NEt₃ followed by crystallization from MeOH-CH₂Cl₂ provided **1** in ~66% yield. On the other hand, the reaction without NEt₃ demanded longer stirring time (>6 h) to get the red-brown solution, and the yield was considerably lower (~20%). The

Table 1 Crystal structure parameters and refinement data for 1·H₂O, 2·H₂O·MeOH, 3·ClO₄·DMSO and 4·ClO₄·DMSO^a

Parameters	Complex 1	Complex 2	Complex 3	Complex 4
Formula	C ₃₀ H ₅₀ Mn ₃ N ₂ O ₁₈	C ₃₂ H ₄₈ Cl ₄ Mn ₃ N ₂ O ₁₈	C ₅₀ H ₇₀ ClMn ₄ N ₇ O ₁₇ S ₃	C ₅₀ H ₇₀ Cl ₂ Mn ₄ N ₄ O ₂₁ S ₃
F.W.	891.54	1055.34	1392.52	1449.94
Crystal system	Triclinic	Monoclinic	Monoclinic	Monoclinic
Space group	<i>P</i> $\bar{1}$	<i>P</i> 2 ₁ / <i>c</i>	<i>P</i> 2 ₁ / <i>c</i>	<i>P</i> 2 ₁ / <i>c</i>
Crystal color	Brown	Brown	Brown	Brown
Crystal size/mm ³	0.32 × 0.26 × 0.21	0.31 × 0.25 × 0.20	0.35 × 0.29 × 0.26	0.34 × 0.26 × 0.23
<i>a</i> /Å	9.875(2)	11.357(6)	11.9220(9)	11.6789(18)
<i>b</i> /Å	10.924(2)	10.602(5)	12.4025(9)	45.485(7)
<i>c</i> /Å	11.134(2)	18.852(9)	42.763(3)	16.2162(19)
α /°	95.459(6)	90.00	90.00	90.00
β /°	114.801(5)	106.516(16)	96.768(2)	131.030(7)
γ /°	111.466(5)	90.00	90.00	90.00
<i>V</i> /Å ³	969.7(3)	2176.3(19)	6279.0(8)	6498.3(16)
<i>Z</i>	1	2	4	4
<i>D</i> _c /g cm ⁻³	1.527	1.610	1.473	1.482
μ (mm ⁻¹)	1.037	1.176	0.998	1.010
<i>F</i> (000)	463	1082	2880	2992
<i>T</i> /K	298(2)	298(2)	298(2)	298(2)
Total reflns	13 150	23 774	79 807	62 705
<i>R</i> (int)	0.0347	0.1447	0.1150	0.0927
Unique reflns	4739	4983	12 849	11 634
Observed reflns	3236	3280	6961	7070
Parameters	269	289	739	761
<i>R</i> ₁ ; <i>wR</i> ₂ (<i>I</i> > 2σ(<i>I</i>))	0.0395, 0.1032	0.0788, 0.2346	0.0755, 0.2351	0.0828, 0.2539
GOF (<i>F</i> ²)	1.047	1.034	1.045	1.038
Largest diff peak and hole (e Å ⁻³)	0.424, -0.499	1.687, -1.242	1.622, -0.923	2.029, -1.192

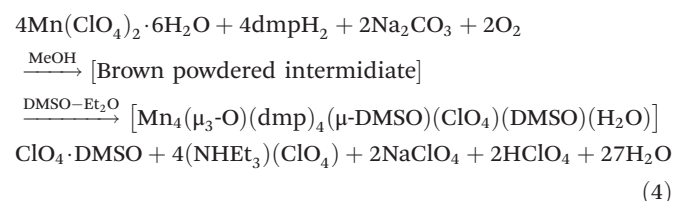
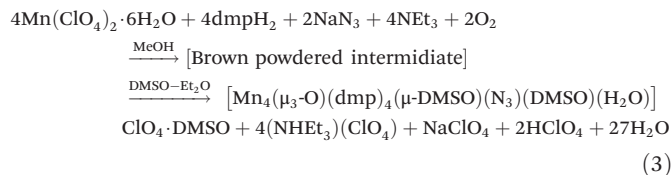
$$^a R_1 = \sum(|F_o| - |F_c|) / \sum|F_o|, wR_2 = [\sum w(|F_o| - |F_c|)^2 / \sum w(F_o)^2]^{1/2}, w = 0.75 / (\sigma^2(F_o) + 0.0010F_o^2)$$

same reaction using ClCH₂CO₂Na in place of MeCO₂Na led to compound **2** in 59% yield. The chemical reactions for the generation of **1** and **2** are summarized in eqn (1) and (2) below.



During the formation of **1** and **2** in the solution, most likely the single phenoxido coordination initially forms the mononuclear trivalent species [Mn^{III}(dmp)(carboxylate)(H₂O)₂]. Simultaneously, if a [Mn^{II}(carboxylate)₂] species is also formed in the solution, two [Mn^{III}(dmp)(carboxylate)(H₂O)₂] species can trap it to yield **1** and **2** depending on the carboxylates used (Schemes S2 and S3, ESI†). Thus, the structure is composed of two terminal mononuclear units of [Mn^{III}(dmp)(RCOO)(H₂O)] connected by a central [Mn^{II}(RCOO)₂] unit through the alkoxido oxygen atoms of the ligand and the oxygen atoms of carboxylate anions. We have tried another reaction using NaN₃ in place of sodium carboxylates in the previous reactions (1) and (2). The reaction of Mn(ClO₄)₂, ligand, NaN₃ and NEt₃ in 2 : 2 : 2 : 1 molar ratio in MeOH in air produced a red-brown powder in 62% yield. Several pure and mixed organic solvents

were employed to grow X-ray diffraction quality single crystals of this red-brown product. Only a 1 : 1 DMSO-Et₂O mixture afforded brown single crystals of **3** in 24% yield after two months, and X-ray analysis established it as [Mn₄(μ₃-O)-(dmp)₄(μ-DMSO)(N₃)(DMSO)(H₂O)]ClO₄·DMSO. The presence of the single anionic fragment within the tetranuclear aggregate was further confirmed by an analogous reaction using Na₂CO₃ in place of NaN₃. The reaction of Mn(ClO₄)₂, H₂dmp, and Na₂CO₃ in a 2 : 2 : 1 molar ratio in MeOH initially afforded the powder material, which on treatment with a 1 : 1 DMSO-Et₂O solvent mixture afforded [Mn₄(μ₃-O)(dmp)₄(μ-DMSO)(ClO₄)(DMSO)(H₂O)]·ClO₄·DMSO (**4**) in 18% yield. The DMSO-Et₂O (1 : 1) solvent mixture is a unique one for the slow and smooth recrystallization process. The reactions for the generation of **3** and **4** are summarized in eqn (3) and (4), respectively.



A different type of aggregation process took place to provide $[\text{Mn}_4]$ coordination clusters **3** and **4** in the absence of carboxylates and in the presence of azide and perchlorate anions. Initially in the solution, the most probable precursor species formed is $[\text{Mn}^{\text{III}}(\text{dmp})(\text{ClO}_4)(\text{H}_2\text{O})_2]$. In the following step, DMSO as solvent of crystallization coordinates in two different modes to the Mn centers and plays a crucial role for $[\text{Mn}_4]$ aggregate formation. In these two aggregates, two DMSO groups are present as neutral monodentate and bridging O donor ligands (Schemes S3 and S4, ESI†).²¹

The elemental analysis of solid samples and molar conductivity studies in respective solutions also conform to the above-mentioned formulas of the four compounds. The nature and composition of the final complex is thus greatly influenced by the presence of the ancillary ligands and crystallizing solvent pair.

FT-IR spectra

All three complexes exhibit characteristic stretching frequencies for the dmp^{2-} ligand anion bound to the manganese centers (Fig. S1 and S2, ESI†). The $\tilde{\nu}_{\text{C}=\text{N}}$ stretching vibrations of manganese-bound imine functionalities are observed at 1601–1618 cm^{-1} for **1–4**. For **1** and **2**, the asymmetric $\tilde{\nu}_{\text{as}(\text{COO})}$ stretching vibrations of the four bound carboxylate groups are detected at 1562 and 1570 cm^{-1} , respectively, while the symmetric ($\tilde{\nu}_{\text{s}(\text{COO})}$) stretching vibrations are observed at 1411 and 1385 cm^{-1} , respectively. The differences in these two types of stretching frequencies ($\Delta\tilde{\nu} = \tilde{\nu}_{\text{as}(\text{COO})} - \tilde{\nu}_{\text{s}(\text{COO})}$) are 151 and 185 cm^{-1} , respectively, which are characteristic of the $\mu_{1,3}$ -bridging carboxylates in **1** and **2**.²² In complex **3**, a strong band at 2027 cm^{-1} is assigned to the asymmetric stretching vibration, $\nu_{\text{as}(\text{NNN})}$, of the azide group terminally bound to the Mn^{III} center.²³ Characteristic stretching vibrations for the $[\text{Mn}_3\text{O}]$ base units were observed at 663 and 615 cm^{-1} for **3** and **4**, respectively.²⁴ In addition to these, very strong bands at ~ 1095 cm^{-1} for **3** and **4** are attributed to the uncoordinated ClO_4^- anions. For **4**, the stretching frequencies for one coordinated ClO_4^- ion appear at 1203, 1182 and 1130 cm^{-1} , corresponding to the triply degenerate ν_3 mode of vibration of the tetrahedral ClO_4^- ion.²⁵ Another characteristic set of resonances at 1027 and 762 cm^{-1} in **3** and 1045 and 722 cm^{-1} in **4** was assigned to the $\nu_{\text{as}(\text{S}-\text{O})}$ and $\nu_{\text{as}(\text{C}-\text{S})}$ asymmetric stretching vibrations of DMSO molecules. The $\nu_{\text{as}(\text{S}-\text{O})}$ stretching fre-

quency for free DMSO appears at 1055 cm^{-1} , which is shifted to low energy by 27 and 10 cm^{-1} for **3** and **4**, respectively.²⁶ This shift in S–O stretching frequencies also confirms the monodentate and bridging coordination of DMSO molecules through their oxygen atoms.²⁷

Electronic spectra

The electronic absorption spectra of $[\text{Mn}_3]$ and $[\text{Mn}_4]$ complexes have been measured in MeCN. Complexes **3** and **4** exhibit absorption shoulders around 575 nm for the manganese(III)-based d–d transition.²⁸ The intensities of the other manganese based d–d transition are very low and observed at 382–390 nm with ϵ values of 4785–10 610 $\text{M}^{-1} \text{cm}^{-1}$ for all four complexes. The bands in the range of 400–200 nm are likely to be of charge-transfer origin. In MeCN solutions, the band below 300 nm *viz.*, at 233 (ϵ , 42 625 $\text{M}^{-1} \text{cm}^{-1}$), 236 (ϵ , 48 910 $\text{M}^{-1} \text{cm}^{-1}$), 256 (ϵ , 13 295 $\text{M}^{-1} \text{cm}^{-1}$) and 260 nm (ϵ , 13 970 $\text{M}^{-1} \text{cm}^{-1}$) for **1–4**, respectively, originate from the $\pi \rightarrow \pi^*$ transitions associated with the azomethine group.²⁹

Crystal structures description

1·2H₂O and 2·H₂O·MeOH. The structures of mixed valence neutral units $[\text{Mn}_3(\text{O}_2\text{CMe})_4(\text{dmp})_2(\text{H}_2\text{O})_2]$ and $[\text{Mn}_3(\text{O}_2\text{CCH}_2\text{Cl})_4(\text{dmp})_2(\text{H}_2\text{O})_2]$ in **1** and **2**, respectively, are shown in Fig. 1 and selected bond distances and angles are summarized in Table 2 and S1 (ESI†). Complex **1** crystallizes in the triclinic $P\bar{1}$ space group, while **2** crystallizes in the monoclinic $P2_1/c$ space group. The central manganese ion is located at a crystallographic inversion center. Each dmp^{2-} provides a tridentate ONO donor chelation mode to a terminal Mn^{III} ion (Mn1), wherein an alkoxido O atom bridges to the central Mn^{II} ion (Mn2). Each $\text{Mn}^{\text{III}}\text{Mn}^{\text{II}}$ pair is also bridged by two $\eta^1:\eta^1:\mu$ -acetato linkers, which complete the hexa-coordinate environments around three Mn ions. The structural analyses reveal a linear $\text{Mn}^{\text{III}}\text{Mn}^{\text{II}}\text{Mn}^{\text{III}}$ unit with a $\text{Mn}\cdots\text{Mn}\cdots\text{Mn}$ angle of 180° (Fig. S3, ESI†). The Mn oxidation states were evident from the metric parameters and the Jahn–Teller axial elongation at the two terminal Mn^{III} ions along Mn1–O6 (2.207, 2.242 Å) and Mn1–O7 (2.340, 2.255 Å) bonds, and were confirmed by BVS calculations (Table S2, ESI†).³⁰ The identification of the Jahn–Teller axis on each Mn^{III} center defines the *basal* plane consisting of O1, O2, O4 and N1 atoms with distances within the range of 1.873–2.004 Å for **1** and **2**.

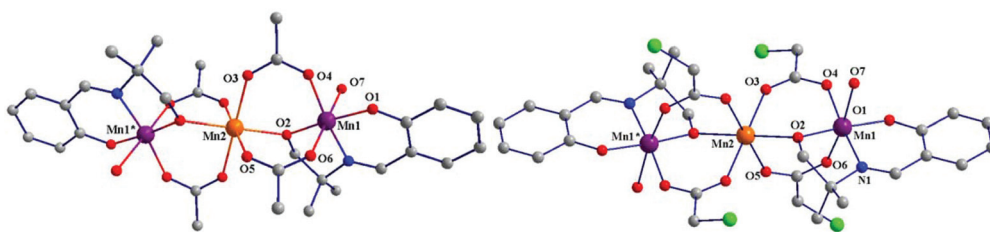


Fig. 1 Structure of the neutral trinuclear units of **1** (left) and **2** (right) with partial atom-numbering scheme. H atoms and lattice solvent molecules have been omitted for clarity. Color code: Mn^{III}, purple; Mn^{II}, orange; O, red; N, blue; C, grey; Cl, green.

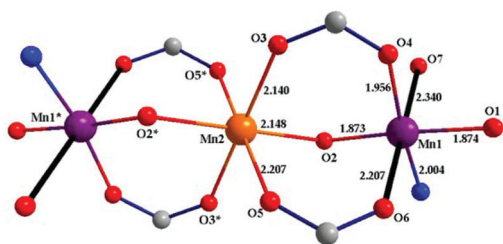


Fig. 2 Core structure of **1** (with unique bond distances in Å), with the O–Mn–O Jahn–Teller axes on the terminal atoms indicated as black bonds. Color code: Mn^{III}, purple; Mn^{II}, orange; O, red; N, blue; C, grey. Atoms labeled with * were generated from the parent atoms by inversion through the Mn2 center.

For these two complexes, the Mn–O_{carb} (carb = carboxylate) distances from manganese in +2 and +3 oxidation states for $\mu_3:\eta^1:\eta^1$ -carboxylato bridges fall within a 1.956–2.246 Å range. The Mn^{III}–O_{carb} distances are shorter (1.956–2.207 Å) compared to the Mn^{II}–O_{carb} distances (2.140–2.207 Å). Around the central Mn^{II} atom, the O₆ environment is less distorted (the angles between *cis* atoms are 87.5–92.5° and *trans* atoms is 180°) compared to the terminal NO₅ environments (angles between *cis* and *trans* atoms range in 83.4–98.5° and 170.2–179.5°, respectively) (Fig. 2). In complex **1**, the Mn(1)···Mn(2) and Mn(1)···Mn(1*) distances of 3.476(7) and 6.953(1) Å, respectively, are shorter than those in **2** at 3.520(2) and 7.040 Å, respectively.

The analysis of the crystal packing of the trinuclear complexes **1** and **2** reveals the presence of extensive noncovalent interactions. One water molecule in **1** and one water and one MeOH molecule in **2** are present as solvent of crystallization. The packing diagram for **1** along the *a* axis shows well-isolated trinuclear complexes that are organized in layers with the water molecules occupying the space within these layers. The closest intermolecular Mn···Mn distances between adjacent layers are 7.150 and 9.515 Å for **1** and **2**, respectively. The intermolecular separations within the same layer are 6.576 and 5.406 Å for **1** and **2**, respectively (Fig. 3). There are hydrogen bonding interactions, involving the bridging acetate ligands

Table 2 Selected bond distances (Å) of complexes **1**·2H₂O and **2**·H₂O·MeOH

Complex 1 ·2H ₂ O			
Mn1–O2	1.873(16)	Mn1–O7	2.340(2)
Mn1–O1	1.873(17)	Mn2–O3	2.140(19)
Mn1–O4	1.956(18)	Mn2–O2	2.148(16)
Mn1–N1	2.004(2)	Mn2–O5	2.206(19)
Mn1–O6	2.2073(19)	Mn1···Mn2	3.477(5)
Complex 2 ·H ₂ O·MeOH			
Mn1–O1	1.868(4)	Mn1–O7	2.255(6)
Mn1–O2	1.868(4)	Mn2–O2	2.131(4)
Mn1–O4	1.976(4)	Mn2–O5	2.189(5)
Mn1–N1	1.997(5)	Mn2–O3	2.153(4)
Mn1–O6	2.244(5)	Mn1···Mn2	3.522(1)

and the lattice water molecules. The complexes further show strong π ··· π (phenyl) interaction between the neighboring Mn₃ units (Fig. 3). The distance between H7 of one phenyl ring and the phenyl ring of next layer is 3.261 Å.

The type of linear Mn₂^{III}Mn^{II} arrangement reported in this study for **1** and **2** is rare in the literature.³¹ The Mn₂^{II}Mn^{III} core is known in two earlier examples, one of which is a SMM.^{31–33} There are other examples of linear Mn₃ units in other combinations of oxidation states, which include Mn₃^{II,34} Mn^{II}Mn^{III}Mn^{IV},³⁵ and Mn₃^{IV}.³⁶

3-ClO₄·DMSO and 4-ClO₄·DMSO. The tetranuclear structures of cationic fragments [Mn₄^{III}(μ_3 -O)(μ -dmp)₄(μ -DMSO)(DMSO)(X)(H₂O)]⁺ (X = N₃⁻ and ClO₄⁻) in **3** and **4**, respectively) are shown in Fig. 4 and selected inter atomic distances and angles are summarized in Table 3 and S3 (ESI[†]). Complexes **3** and **4** crystallize in the monoclinic *P*2₁/*c* space group and the asymmetric units for the two compounds contain the whole Mn₄ unit, *i.e.*, one perchlorate counter anion and one DMSO molecule as solvent of crystallization. Each dmp²⁻ shows tridentate chelation to one of the four Mn^{III} ions present in the cluster with terminal alkoxido group bridging to the adjacent Mn^{III} ions (Fig. 5). The asymmetric cationic units consist of a planar triangular Mn₃^{III} unit tightly bridged by a central μ_3 -O

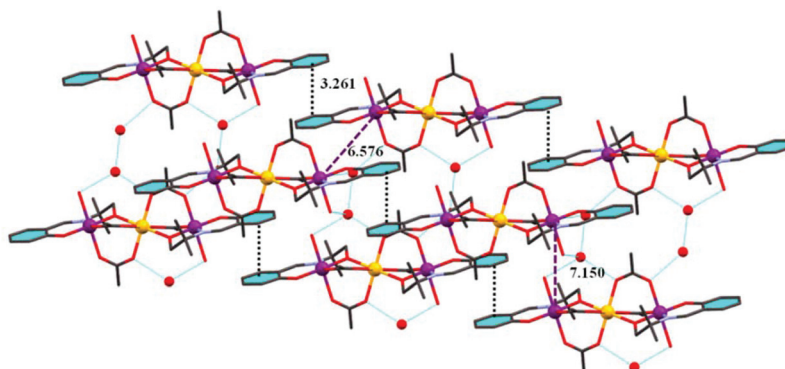


Fig. 3 H-bonding and π – π interaction present in complex **1**.

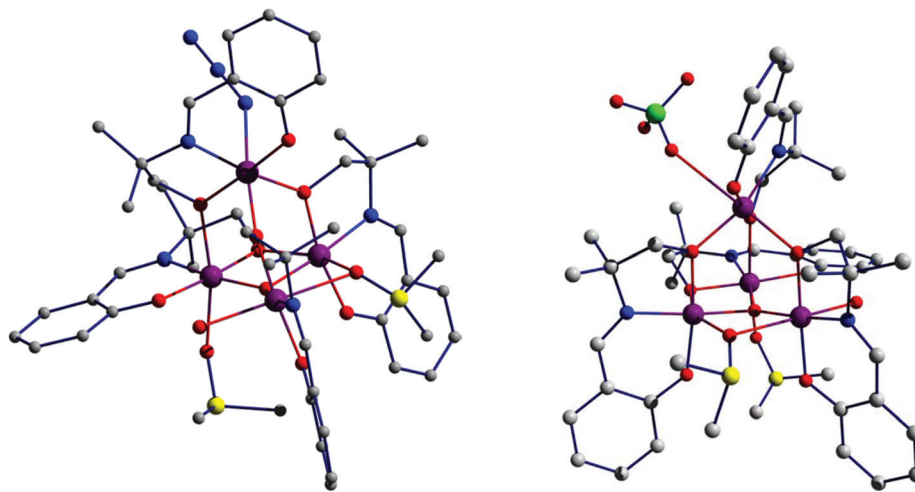


Fig. 4 Structure of the cationic tetranuclear units of **3** (left) and **4** (right). H atoms and lattice solvent molecules have been omitted for clarity. Color code: Mn^{III}, purple; O, red; N, blue; C, grey; S, yellow.

atom derived from a solvent water molecule. For compound **3**, this $\mu_3\text{-O}^{2-}$ ion lays 0.118 Å below the plane of the three Mn ions. The $[\text{Mn}_3\text{O}]$ unit accepts the fourth Mn atom through one alkoxido bridge donation and two alkoxido bridge acceptances from the Mn^{III} bound ligand alcohol arms. Two solvent DMSO molecules show bridging and terminal coordination to three Mn ions within the $[\text{Mn}_3\text{O}]$ entity. Finally, one $\text{N}_3^-/\text{ClO}_4^-$ ion and one solvent water molecule on two Mn ions complete the six-coordination environment around each Mn ion. The μ_3 -oxido supported $[\text{Mn}_3]$ unit attaches to the fourth Mn atom (Mn4) through acceptance of two ligand alkoxido (O_{alk}) bridges of ligand bound Mn2 and Mn3 centers, and donation of its own ligand alkoxido (O_{alk}) bridge to Mn1.

The *cis* and *trans* angles vary within 76.2–101.8 and 155.3–174.9°, respectively, which clearly indicate the distortions within the tetranuclear molecules resulting in strained structures (Table S2, ESI[†]). Both compounds thus contain a pseudo-adamantane $[\text{Mn}_4\text{O}_{10}]$ unit supported by oxido, alkoxido and DMSO bridges. The Mn oxidation states were confirmed by BVS calculations (Table S2, ESI[†]). As expected, all four Mn^{III} centers exhibit Jahn–Teller axial elongation along the O7–Mn1–O11, O4–Mn2–O9, O1–Mn3–O2 and N5–Mn4–O8 (O13–Mn4–O8 in case of complex **4**) axes with bond distances in the range from 2.174 to 2.732 Å (Fig. S4[†]). The oxido nucleus of the $[\text{Mn}_3\text{O}]$ unit registers shorter Mn–O distances in the 1.894–1.927 Å range and is responsible for three Mn···Mn separations of 2.997 to 3.516 Å within this unit. The fourth Mn ion, in this pseudo-adamantane structure, records three other Mn···Mn distances at 3.550, 3.670 and 3.671 Å (Fig. 8a). All these distances are close to other reported μ_4 -oxido bridged $[\text{Mn}_4\text{O}]$ units showing Mn···Mn distances in the 2.819–3.734 Å range.³⁷

The asymmetric nature of the μ_3 -oxido bridge is confirmed from the varying magnitudes of Mn–O–Mn angles in the 102–136° range. Three Mn^{III} ions in the $[\text{Mn}_3\text{O}]$ unit are in

Table 3 Selected bond distances (Å) for **3**·ClO₄·DMSO and **4**·ClO₄·DMSO

3·ClO ₄ ·DMSO			
Mn1–O3	1.884(4)	Mn3–O1	1.877(5)
Mn1–O10	1.911(4)	Mn3–O2	1.938(4)
Mn1–O11	2.247(4)	Mn3–O3	2.174(4)
Mn1–N1	1.989(5)	Mn3–O4	2.324(4)
Mn1–O6	1.899(4)	Mn3–O6	1.927(4)
Mn1–O7	2.302(5)	Mn3–N3	1.998(5)
Mn2–O4	2.417(5)	Mn4–O2	1.973(4)
Mn2–O5	1.893(4)	Mn4–O8	2.203(4)
Mn2–O6	1.894(4)	Mn4–O11	1.878(4)
Mn2–O8	1.889(4)	Mn4–O12	1.877(5)
Mn2–O9	2.239(5)	Mn4–N4	2.016(5)
Mn2–N2	2.000(5)	Mn4–N5	2.325(6)
Mn1···Mn2	3.516(9)	Mn2···Mn4	3.671(6)
Mn1···Mn3	2.997(13)	Mn1···Mn4	3.670(6)
Mn2···Mn3	3.228(14)	Mn3···Mn4	3.550(1)
4·ClO ₄ ·DMSO			
Mn1–O7	2.282(6)	Mn3–O1	1.881(5)
Mn1–O10	1.916(5)	Mn3–O2	1.959(5)
Mn1–O11	2.252(5)	Mn3–O3	2.175(5)
Mn1–N1	2.000(6)	Mn3–O4	2.349(6)
Mn1–O6	1.906(5)	Mn3–O6	1.919(5)
Mn1–O3	1.890(5)	Mn3–N3	1.996(6)
Mn2–O4	2.431(6)	Mn4–O12	1.876(6)
Mn2–O5	1.886(6)	Mn4–O8	2.129(5)
Mn2–O6	1.895(5)	Mn4–O11	1.866(5)
Mn2–O8	1.891(5)	Mn4–O13	2.732(9)
Mn2–O9	2.227(6)	Mn4–N4	2.001(6)
Mn2–N2	1.997(6)	Mn4–O2	1.955(5)
Mn1···Mn2	3.532(6)	Mn2···Mn4	3.587(1)
Mn1···Mn3	2.990(16)	Mn1···Mn4	3.654(7)
Mn2···Mn3	3.233(16)	Mn3···Mn4	3.505(1)

NO₅ environment, whereas the fourth one has N₂O₄ surroundings (Fig. 5). Interestingly, the DMSO molecules showed two types of binding modes, which are not routinely seen in other

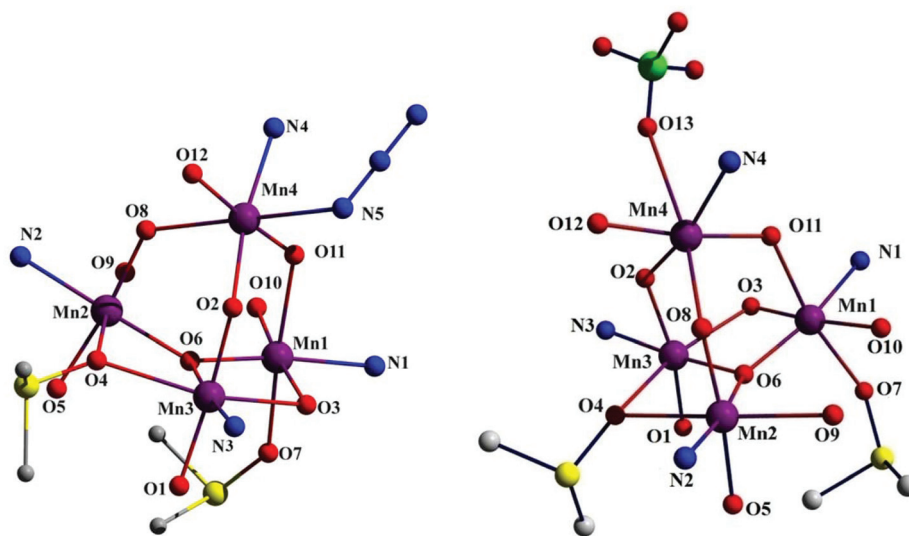


Fig. 5 The atom connectivity in the core of $3\cdot\text{ClO}_4\cdot\text{DMSO}$ (left) and $4\cdot\text{ClO}_4\cdot\text{DMSO}$ with partial atom numbering schemes. Color code: same as Fig. 4.

known manganese coordination aggregates, one in a monodentate O donor mode and the other in a $\mu_{1,1}\text{-O}$ fashion.³⁸ The monodentate azide N and perchlorate O atoms show weak and distal binding to the fourth Mn ion at 2.325 and 2.732 Å in **3** and **4**, respectively. The terminally bound water molecules of Mn2 centers were engaged in intramolecular H-bonding interactions with the Mn1 bound phenoxido O atoms in **3** and **4** at 2.697 and 2.704 Å, respectively (Fig. S5, ESI†).

Magnetic properties

Given the structural and chemical similarity in the pairs of trinuclear complexes **1** and **2** and tetranuclear complexes **3** and **4**, we present and discuss the magnetic behavior for complexes **1** and **2** first, followed by the discussion of magnetism for complex **3**.

1·2H₂O and 2·H₂O·MeOH. These complexes contain the central high-spin Mn^{II} ion ($S = 5/2$) and two peripheral high-spin Mn^{III} ions ($S = 2$ each), which provide the expected spin-only value of $\chi T = 10.38 \text{ emu mol}^{-1} \text{ K}$ in the absence of magnetic exchange. Temperature-dependent magnetic susceptibility measurements (Fig. 6) revealed that at 300 K, the χT values for both **1·2H₂O** and **2·H₂O·MeOH** are lower, *i.e.*, 8.46 and 10.36 $\text{emu mol}^{-1} \text{ K}$, respectively. In both cases, the χT curve exhibits a substantial decrease as the temperature is lowered. These observations are in accord with antiferromagnetic exchange interactions between the central Mn^{II} ion and the peripheral Mn^{III} ions. Fitting the high-temperature part of the inverse susceptibility plot to the Curie–Weiss law afforded the values of the Curie (C) and Weiss (θ) constants, $C = 12.32(8) \text{ emu mol}^{-1} \text{ K}$ and $\theta = -134(2) \text{ K}$ for **1·2H₂O** and $C = 12.75(4) \text{ emu mol}^{-1} \text{ K}$ and $\theta = -67.0(8) \text{ K}$ for **2·H₂O·MeOH**. The Curie constants are similar and significantly higher than the sum of expected spin-only values for uncoupled $S = 5/2$ and two $S = 2$ centers. This difference can be explained by the

orbital contribution to the total moment of the Mn^{III} ion. The negative Weiss constants are in agreement with the antiferromagnetic exchange coupling in the trimers, with the exchange interaction in **1·2H₂O** being stronger than in **2·H₂O·MeOH**.

The magnetic properties of the trimers were modeled using the Heisenberg–Dirac–Van Vleck Hamiltonian (1),

$$\hat{H} = -2J_1(\hat{S}_1\hat{S}_2 + \hat{S}_2\hat{S}_3) - 2J_2\hat{S}_1\hat{S}_3 + \sum_i \mu_B g_i \hat{S}_i \vec{H}, \quad (1)$$

where S_1, S_2, S_3 are the spin states and g_1, g_2, g_3 are the g -factors of Mn^{III}, Mn^{II}, and Mn^{III} ions, respectively, J_1 is the exchange coupling constant for the interaction between the central Mn^{II} and peripheral Mn^{III} ions, and J_2 is the weaker interaction between the peripheral Mn^{III} ions. The mean-field correction (zJ') was also included to account for intermolecular dipolar coupling at lower temperatures. To avoid overparametrization during the fitting procedure, it was reasonably assumed that $g_2 = 2.00$ and $J_2 = 0$ based on the earlier reports of magnetic behavior for similar trinuclear Mn^{III}–Mn^{II}–Mn^{III} clusters.^{39–43} In addition, $g_1 = g_3 = g$ due to the symmetry of the clusters **1** and **2**. The best fit to the experimental data was obtained with $J_1 = -7.36(2) \text{ cm}^{-1}$, $g = 2.11(1)$, $zJ' = -0.26(1) \text{ cm}^{-1}$ for **1·2H₂O** ($R^2 = 0.9997$). In the case of **2·H₂O·MeOH**, however, the three-parameter model could not provide a satisfactory fit to the data, and therefore the g_2 parameter was also allowed to vary, which led to an acceptable fit with $J_1 = -5.04(6) \text{ cm}^{-1}$, $g = 2.38(1)$, $g_2 = 1.84(1)$, $zJ' = -0.079(5) \text{ cm}^{-1}$ ($R^2 = 0.9976$). The refined g_2 value, however, is somewhat low and atypical for the high-spin Mn^{II} ion.

Both **1** and **2** exhibit antiferromagnetic nearest-neighbor exchange interactions that result in the ground state spin of $3/2$. The more negative value of the J_1 exchange constant observed for cluster **1** can be explained by the shorter separation between the Mn^{II} and Mn^{III} centers in **1** (3.477 Å) as com-

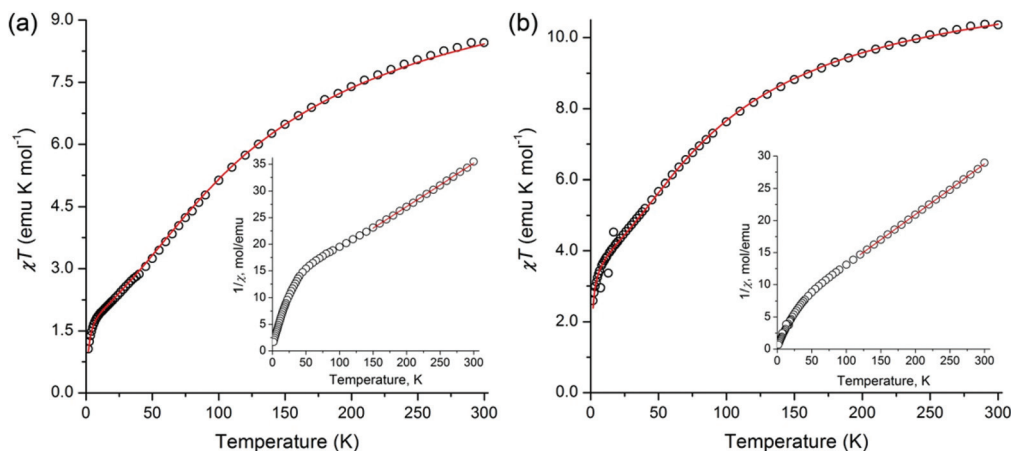


Fig. 6 The temperature dependence of χT for (a) $1 \cdot 2\text{H}_2\text{O}$ and (b) $2 \cdot \text{H}_2\text{O} \cdot \text{MeOH}$. The solid red lines represent the best fit to the experimental data. The insets show the corresponding temperature dependence of inverse susceptibility and the fit to the Curie–Weiss law in the high-temperature region (solid red lines).

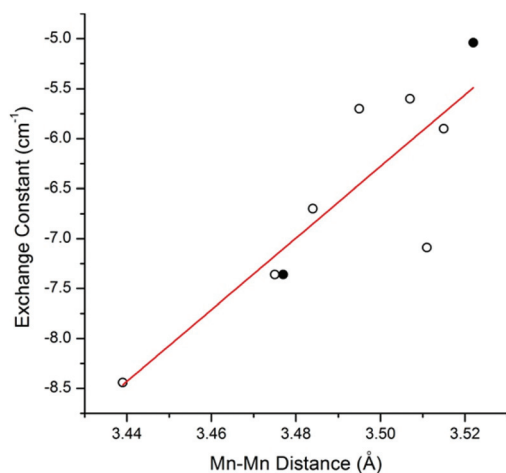


Fig. 7 The magnetic exchange constant (J_1) between the central Mn^{II} and peripheral Mn^{III} ions in the carboxylate-supported $\text{Mn}^{\text{III}}\text{–Mn}^{\text{II}}\text{–Mn}^{\text{III}}$ trimers as a function of the $\text{Mn}^{\text{II}}\text{...Mn}^{\text{III}}$ separation. The data established in this study are indicated with filled circles.

pared to **2** (3.522 Å). Indeed, an examination of the correlation between J_1 and the $\text{Mn}^{\text{II}}\text{...Mn}^{\text{III}}$ separation in these and related carboxylate-supported $\text{Mn}^{\text{III}}\text{Mn}^{\text{II}}\text{Mn}^{\text{III}}$ trimers revealed that this relationship can be described, rather approximately, as $J_1 = A + Bd$ ($\text{Mn}^{\text{II}}\text{...Mn}^{\text{III}}$), where $A = -1.3(3) \times 10^2 \text{ cm}^{-1}$ and $B = 36(8) \text{ cm}^{-1}/\text{\AA}$ (Fig. 7). We note that the $\text{Mn}^{\text{II}}\text{...Mn}^{\text{III}}$ separation in **2** is one of the longest observed in such trimers. This observation might explain the imperfection of the presented isotropic model for the treatment of magnetism in complex **2** and the somewhat abnormal value of the g_2 parameter.

3·ClO₄·DMSO. The paramagnetic core in cluster **3** contains four high-spin Mn^{III} ions ($S = 2$ each) with irregular $\text{Mn}\text{...Mn}$ separations (Fig. 8a). Similar to clusters **1** and **2**, the temperature dependence of χT for **3** reveals significant antiferromagnetic correlations (Fig. 9), with the room-temperature value of $11.05 \text{ emu mol}^{-1} \text{ K}$. Fitting the high-temperature part of the inverse susceptibility plot to the Curie–Weiss law resulted in $C = 12.9(3) \text{ emu mol}^{-1} \text{ K}$ and $\theta = -48(7) \text{ K}$ (Fig. 9, inset). The Curie constant (C) is slightly higher than the spin-

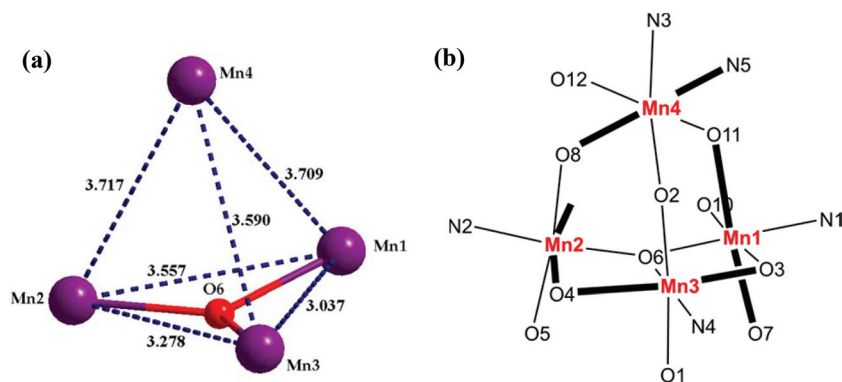


Fig. 8 (a) $\text{Mn}\text{...Mn}$ distances within the labeled core of **3**; (b) the nearest environment of octahedrally coordinated Mn^{III} ions, with the elongated Jahn–Teller axes highlighted as bold bonds.

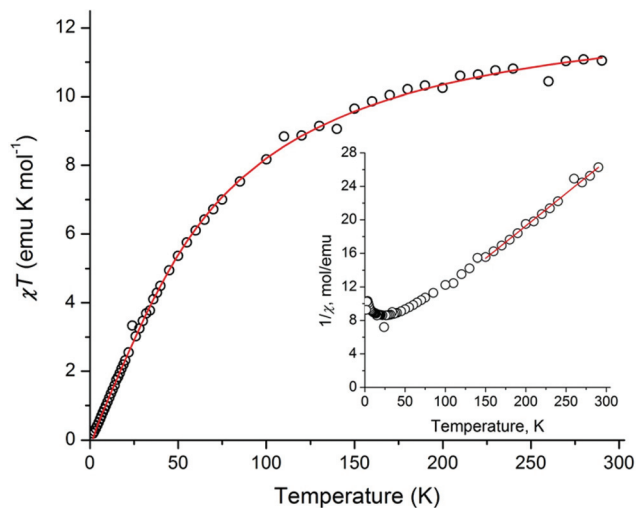


Fig. 9 The temperature dependence of χT for $3 \cdot \text{ClO}_4 \cdot \text{DMSO}$. The solid red line represents the best fit to the experimental data. The inset shows the temperature dependence of inverse susceptibility and the fit to the Curie–Weiss law in the high-temperature region (solid red line).

only expectation value for four uncoupled $S = 2$ centers ($12.0 \text{ emu mol}^{-1} \text{ K}$). The discrepancy is attributed to the orbital contribution of the Mn^{III} ion. The negative Weiss constant (θ) indicates dominant antiferromagnetic exchange coupling between the Mn^{III} centers, which results in the χT quickly decreasing below 100 K and approaching zero at 1.8 K.

The strength of magnetic coupling in clusters with octahedral high-spin Mn^{III} ions strongly depends on the orientation of the elongated Jahn–Teller axis that defines the magnetic σ -type 3d orbital.⁴⁴ An examination of the metric parameters in cluster **3** (Table 3) reveals that the $\text{Mn}2\text{--O}4\text{--Mn}3$ superexchange pathway (J_1) involves the magnetic σ -type orbitals on both the Mn^{III} centers, the $\text{Mn}1\text{--O}3\text{--Mn}3$, $\text{Mn}1\text{--O}11\text{--Mn}4$, and $\text{Mn}2\text{--O}8\text{--Mn}4$ pathways (J_2) each involve such an orbital on only one of the Mn^{III} centers, and finally, the $\text{Mn}1\text{--O}6\text{--Mn}2$ and $\text{Mn}3\text{--O}2\text{--Mn}4$ pathways (J_3) do not involve such orbitals at all (Fig. 8b). Each of the six superexchange pathways, however, involves π -type 3d orbitals of the Mn^{III} ions. Based on these symmetry considerations, one could expect antiferromagnetic J_1 and J_3 , as they are dominated by interactions between magnetic orbitals of the same symmetry. The J_2 interaction contains both $\sigma\text{--}\pi$ and $\pi\text{--}\pi$ contributions, and therefore its absolute value is expected to be smaller but its sign cannot be clearly predicted. Consequently, the magnetic behavior of **3** was modeled using three different exchange parameters with the above-set restrictions ($J_1 < 0, J_3 < 0, |J_2| \ll |J_1|$):

$$\hat{H} = -2J_1\hat{S}_2\hat{S}_3 - 2J_2(\hat{S}_1\hat{S}_3 + \hat{S}_1\hat{S}_4 + \hat{S}_2\hat{S}_4) - 2J_3(\hat{S}_1\hat{S}_2 + \hat{S}_3\hat{S}_4) + \sum_i \mu_{\text{B}}g_i\hat{S}_i\hat{H}, \quad (2)$$

where S_i and g_i are the spin state and g -factor of each Mn^{III} ion. To avoid overparameterization, the g_i values were set equal

for all four Mn^{III} centers. The best fit to the experimental data was achieved with $g = 2.085(6)$, $J_1 = -5.2(1) \text{ cm}^{-1}$, $J_2 = 0.098(8) \text{ cm}^{-1}$, and $J_3 = -5.4(1) \text{ cm}^{-1}$ ($R^2 = 0.9989$). We note that the low symmetry of cluster **3** suggests the three- J model used is certainly an oversimplification. Nevertheless, it provides a good fit to the experimental data and allows a reasonable estimate of the magnetic exchange coupling parameters in this complex.

In spite of our several attempts, we are unable to isolate the pure crystals of the complex **4** in bulk form. Therefore, we intentionally exclude the magnetic property of complex **4** here.

Catechol oxidation study

In this study, we examined the ability of our $[\text{Mn}_3]$ and $[\text{Mn}_4]$ assemblies to act as catalysts in the oxidation of 3,5-di-*tert*-butylcatechol (3,5-DTBC) to the corresponding quinone by UV-vis spectrophotometry. Presence of tertiary butyl groups at 3 and 5 positions on the catechol substrate provides low redox potential for oxidation to 3,5-di-*tert*-butylquinone (3,5-DTBQ) while preventing further oxidation and ring-opening reaction.⁴⁵ The formation of 3,5-DTBQ, which exhibits an absorption maximum at $\sim 400 \text{ nm}$, can be monitored for this reaction catalyzed by the manganese complexes.

Complexes **1–4** in $\sim 1 \times 10^{-6} \text{ M}$ solutions were reacted with a 100-fold more concentrated solution of 3,5-DTBC. The time dependent UV-vis spectra of the mixture were obtained in MeCN and MeOH under aerobic conditions up to 1 h. Spectral changes of **1** and **3** in MeCN after addition of 3,5-DTBC are shown in Fig. 10 (Fig. S6 for **2** in the ESI†). In both the cases, the addition of 3,5-DTBC causes a red shift in the absorption band of complexes from 382 nm (for **1**) and 390 nm (for **3**) to 400 nm with a gradual increase of absorption intensity. These results clearly indicate the catalytic oxidation of 3,5-DTBC to 3,5-DTBQ in solution. However, the generation of the quinone band was not observed during the course of the experiment in pure MeOH, which clearly points out that these complexes were not suitable for the oxidation of 3,5-DTBC in MeOH (Fig. S7, ESI†).⁴⁶ Control experiments in MeCN and air using manganese(II) acetate and manganese(II) perchlorate under analogous conditions did not show any oxidation of 3,5-DTBC to 3,5-DTBQ. Within 2 h of mixing of the metal salts and substrate in solution, the reaction did not demonstrate any amount of 3,5-DTBQ formation.

Kinetic study for catechol oxidation

The kinetic study of the oxidation of 3,5-DTBC to 3,5-DTBQ by the complexes **1–4** were carried out by monitoring the growth of the absorbance at 400 nm by the initial rates method. The experiments were done at a constant temperature of $25 \text{ }^\circ\text{C}$ and under aerobic conditions. For a particular complex–substrate mixture, a time scan at the maximum of the quinone band was carried out for a period of 1 h in MeCN. The rate of oxidation is dependent on the substrate concentration, which was examined using 10^{-6} M solutions of **1** and **3** and increasing amounts of 3,5-DTBC (from 10 to 100 equiv.). In all cases, first order dependence was observed at low substrate concen-

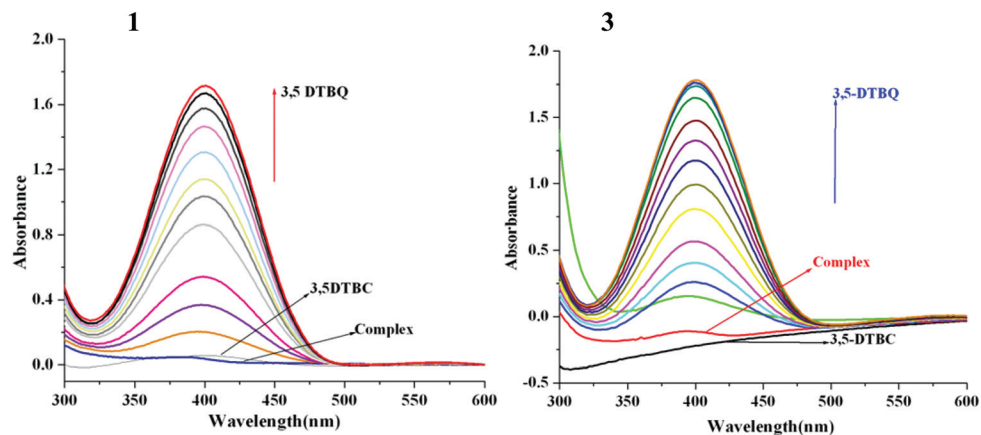


Fig. 10 Increase of absorption spectra after addition of 100 equiv. of 3,5-DTBC to a solution containing complexes **1** (left) and **3** (right) (1×10^{-6} M) in MeCN. The spectra were obtained after every 2 min (for **1**) and 5 min (for **3**) up to 1 h.

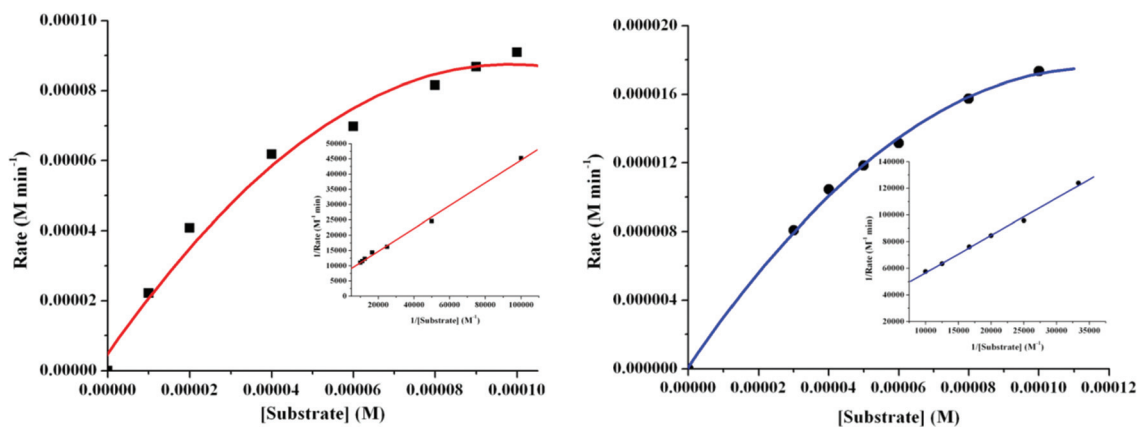


Fig. 11 Plot of initial rates vs. substrate concentration for the oxidation reaction catalyzed by complexes **1** (left) and **3** (right). Inset shows the Lineweaver–Burk plots.

trations, whereas saturation kinetics was found at higher substrate concentrations (Fig. 11) (Fig. S8 in the ESI† for complexes **2** and **4**). The rate constant for a particular complex/substrate mixture was determined from the $\log[A_\alpha/(A_\alpha - A_t)]$ vs. time plot. This type of saturation rate dependence on the concentration of the substrate may be explained by considering the Michaelis–Menten equation for enzymatic kinetics describing the rate of enzymatic reactions by relating the reaction rate to the substrate concentration.⁴⁷ A treatment on the basis of the Michaelis–Menten approach was consequently applied and linearized by means of a Lineweaver–Burk plot (double reciprocal plot) to calculate various kinetic parameters, such as the Michaelis–Menten constant and the maximum rate (V_{\max}) achieved by the system, at maximum (saturating) substrate concentrations.⁴⁸ The Michaelis constant K_m is the substrate concentration, at which the reaction rate is half of V_{\max} and is an inverse measure of the substrate's affinity for the compound behaving as enzyme.

The turnover number (k_{cat}) values can be calculated by dividing the V_{\max} values by the concentration of the corresponding complexes and the kinetic parameters are listed in Table 4. Determination of turnover number (k_{cat}) of the model catalyst is important to understand their relative efficiency. The turnover numbers (k_{cat}) for trinuclear compounds are about four times higher than that of the tetranuclear compound. The title compounds are the first examples of trinuclear mixed-valence $\text{Mn}^{\text{III}}/\text{Mn}^{\text{II}}$ and tetranuclear Mn^{III} compounds showing catechol oxidase activity. The turnover numbers for these complexes are much higher than those found for other manganese complexes.^{49,50}

The mass spectral (ESI-MS positive) characterization of compounds **1**, **3** and **1**:100 mixtures with 3,5-DTBC within 10 min of mixing in MeCN were carried out to get an insight into the nature of possible compound-substrate intermediates for catechol oxidation (Fig. S9–S12, ESI†). Compound **1** exhibits a base peak at $m/z = 194.12$, which can be assigned to the

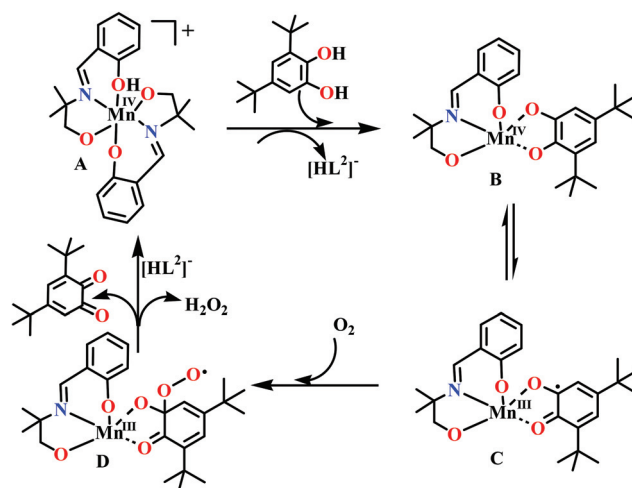
Table 4 Kinetic parameters for compounds 1–4 obtained at 25 °C in a MeCN medium

Compound	V_{\max} ($M s^{-1}$)	Std. error	K_m (M)	Std. error	k_{cat} (h^{-1})
1	1.3717×10^{-4}	2.21×10^{-5}	5.1164×10^{-5}	1.01×10^{-6}	8.220×10^3
2	1.5019×10^{-4}	1.79×10^{-5}	7.4947×10^{-5}	1.32×10^{-6}	9.011×10^3
3	3.4730×10^{-5}	4.89×10^{-5}	9.7106×10^{-5}	9.68×10^{-6}	2.082×10^3
4	3.1092×10^{-5}	7.02×10^{-5}	7.8664×10^{-5}	7.12×10^{-6}	1.865×10^3

protonated ligand $[H_3dmp]^+$ ($C_{11}H_{16}NO_2$). In addition, peaks at $m/z = 438.13$, 287.06 and 246.03 indicate the presence of $[Mn^{IV}(dmp)_2H]^+$ ($C_{22}H_{27}MnN_2O_4$), $[Mn^{II}(dmp)(H_2O)Na]^+$ ($C_{11}H_{15}MnNO_3Na$) and $[Mn^{III}(dmp)]^+$ ($C_{11}H_{13}MnNO_2$), respectively. Compound 3 displays a base peak at $m/z = 324.04$, which can be assigned to the cationic solvent bound species $[Mn^{III}(dmp)(DMSO)]^+$ ($C_{13}H_{19}MnNO_3S$). A common low intensity peak for both the compounds at $m/z = 683.15$ arises due to the dimanganese species $[Mn^{IV}Mn^{III}(dmp)_3]^+$ ($C_{33}H_{39}Mn_2N_3O_6$). The additional peaks in the spectrum of 1 are also present in the spectrum of 3, which indeed confirm the higher stability of the catalytically active mononuclear fragments in MeCN. It is interesting to note that the mass spectra of 1 and 3 are almost same after the addition of 3,5-DTBC. In both cases, the spectra exhibit two peaks at $m/z = 243$ and 463, which correspond to the quinone–sodium aggregates $[(3,5-DTBQ)Na]^+$ ($C_{14}H_{20}O_2Na$) and $[(3,5-DTBQ)_2Na]^+$ ($C_{28}H_{40}O_4Na$), respectively. There is also another peak at $m/z = 466.18$, indicating the presence of the 1 : 1 mononuclear species–substrate aggregates $[Mn^{III}(dmp)(3,5-DTBQ)]^+$ ($C_{25}H_{33}MnNO_4$). Therefore, the ESI-MS spectra allow us to conclude that the complex–substrate intermediates are formed during oxidation reactions by O_2 of air.

Plausible mechanistic considerations of catechol oxidation

On the basis of mass spectrometry evidence, a possible mechanism for the catechol oxidation by compound A ($m/z = 438.13$), as depicted in Scheme 1, is proposed. In the first step of the reaction, the catechol coordinates to A with the removal of one ligand and forms intermediate $[Mn^{IV}(L^2)(3,5-DTBC)]$ (B, $m/z = 466.18$). Internal electron transfer within B produces a semiquinone bound intermediate $Mn^{III}(L^2)(3,5-DTBSQ)$ (C). The species C then reacts with dioxygen from air to generate an oxygenated species (D), which oxidizes the Mn^{III} center and releases 3,5-DTBQ and hydrogen peroxide. After the quinone molecule is released, the ligand then binds to the metal center to regenerate A and the catalytic cycle can continue. Though we could not isolate species C and D from the solution, we proposed this tentative mechanistic cycle that is very much similar to those reported in the literature.⁵¹ The availability of ligand bound Mn^{IV} species in a solution is higher in the case of 1, which leads to higher turn-over number for the experiment.^{31,32} Therefore, it is reasonable to conclude that in the catalytic cycle, ligand bound the Mn^{IV} fragment can undergo two electron reduction with concomitant oxidation of 3,5-DTBC to 3,5-DTBQ in the presence of molecular oxygen.



Scheme 1 Proposed mechanism of catechol oxidation catalyzed by $[Mn^{IV}(dmp)_2H]^+$ (A).

Indeed, several factors must be considered in assessing the difference in oxidation activities of complexes 1–4 such as substrate association affinity, mode of binding of substrate, electrochemical potential values, ancillary donors and steric match. With respect to the catalytic turnover number (k_{cat}), we may conclude that the reactivity in the oxidation of 3,5-DTBC increases in the order $4 < 3 < 2 < 1$.

Conclusion

In summary, we have demonstrated for the first time the use of the same tridentate alcohol-phenol arm bearing ligand, 2-[(2-hydroxy-1,1-dimethyl-ethylimino)-methyl]-phenol, for the growth of two trinuclear $Mn_2^{III}Mn^{II}$ and two tetranuclear Mn_4^{III} complexes 1–4. This study establishes the potential of the ligand in its doubly deprotonated form (both phenol and alcohol end) to enforce the formation of the Mn aggregates of varying nuclearity and contrasting molecular topology. Both the deprotonated alcohol ends are essential for the aggregation of Mn ions. The syntheses of the complexes were explored in detail to identify conditions that led to the specific nuclearity, resulting in either a linear carboxylate-supported trinuclear structure or in an adamantane-like tetranuclear structure built around an oxido-centered Mn_3 triangle. The magnetic behavior of mixed-valent linear trimers 1 and 2 is dominated by anti-ferromagnetic exchange between the central Mn^{II} ion and the

peripheral Mn^{III} ions, which leads to the $S = 3/2$ ground state. A comparison to the related trimers found in the literature revealed that the strength of this exchange coupling correlates well with the Mn^{II}...Mn^{III} separation. The magnetic behavior of the tetranuclear complex **3** is primarily dependent on the orientation of the elongated Jahn–Teller axes of the four octahedrally coordinated Mn^{III} ions. As a result, magnetism is dominated by antiferromagnetic exchange in two different pairs of ions, leading to the overall singlet ground state. Kinetic studies in solution revealed that both the trinuclear and tetranuclear complexes are efficient catalysts for the solvent dependent oxidation of 3,5-di-*tert*-butylcatechol by O₂, with complex **2** being the most active. In MeOH medium, all complexes are characteristically inactive. In MeCN, the reactivity for the oxidation of 3,5-DTBC increases in the order $4 < 3 < 1 < 2$. The ESI-MS (positive) evidences suggest the presence of metal complex–catechol substrate aggregates with bidentate catechol units to Mn centers.

Acknowledgements

We are very much thankful to the reviewers at the revision stage for their valuable and most appropriate suggestions in improving the standard of the manuscript. MP is thankful to the Council of Scientific and Industrial Research, New Delhi, India, for financial support toward her doctoral degree. The authors give thanks to DST, New Delhi, for providing the Single Crystal X-ray Diffractometer facility in the Department of Chemistry, IIT Kharagpur under its FIST program. MP also gives thanks to Dr Debiranjan Tripathy for fruitful discussion. The study on the molecular magnetism by the FSU group was partially supported by the National Science Foundation (award NSF-0911109).

References

- G. E. Kostakis, A. M. Ako and A. K. Powell, *Chem. Soc. Rev.*, 2010, **39**, 2238–2271.
- (a) A. M. Mowson, T. N. Nguyen, A. K. Abboud and G. Christou, *Inorg. Chem.*, 2013, **52**, 12320–12322; (b) M. Sarkar, V. Bertolasi and D. Ray, *Eur. J. Inorg. Chem.*, 2010, 2530–2536.
- (a) M. T. Caudle, J. W. Kamp, M. L. Kirk, P. G. Rasmussen and V. L. Pecoraro, *J. Am. Chem. Soc.*, 1997, **119**, 9297–9298; (b) F. Habib, G. Brunet, F. Loiseau, T. Pathmalingham, T. J. Burchell, A. M. Beauchemin, W. Wernsdorfer, R. Clérac and M. Murugesu, *Inorg. Chem.*, 2013, **52**, 1296–1303.
- (a) K. N. Ferreira, T. M. Iverson, K. Maghlaoui, J. Barber and S. Iwata, *Science*, 2004, **303**, 1831–1838; (b) T. G. Carrell, A. M. Tyryshkin and G. C. J. Dismukes, *Biol. Inorg. Chem.*, 2002, **7**, 2–22; (c) R. M. Cinco, A. Rompel, H. Visser, G. Aromí, G. Christou, K. Sauer, M. P. Klein and V. K. Yachandra, *Inorg. Chem.*, 1999, **38**, 5988–5998; (d) V. K. Yachandra, K. Sauer and M. P. Klein, *Chem. Rev.*, 1996, **96**, 2927–2950.
- V. L. Pecoraro, *Manganese Redox Enzymes*, VCH, New York, 1992.
- A. Zouni, H. T. Witt, J. Kern, P. Fromme, N. Krauss, W. Saenger and P. Orth, *Nature*, 2001, **409**, 739–743.
- N. Kamiya and J. R. Shen, *Proc. Natl. Acad. Sci. U. S. A.*, 2003, **100**, 98–103.
- (a) K. N. Ferreira, T. M. Iverson, K. Maghlaoui, J. Barber and S. Iwata, *Science*, 2004, **303**, 1831–1838; (b) J. Biesiadka, B. Loll, J. Kern, K.-D. Irrgang and A. Zouni, *Phys. Chem. Chem. Phys.*, 2004, **6**, 4733–4736.
- S.-Y. Chen, C. C. Beedle, P.-R. Gan, G.-H. Lee, S. Hill and E.-C. Yang, *Inorg. Chem.*, 2012, **51**, 4448–4457.
- A. Saha, K. A. Abboud and G. Christou, *Inorg. Chem.*, 2011, **50**, 12774–12784.
- P.-P. Yang, C.-Y. Shao, L.-L. Zhu and Y. Xu, *Eur. J. Inorg. Chem.*, 2013, 5288–5296.
- L. Zhang, C. I. Onet, R. Clérac, M. Rouzières, B. Marzec, M. Boese, M. Venkatesan and W. Schmitt, *Chem. Commun.*, 2013, **49**, 7400–7402.
- P. Kar, Y. Ida, T. Kanetomo, M. G. B. Drew, T. Ishida and A. Ghosh, *Dalton Trans.*, 2015, **44**, 9795–9804.
- (a) P. Wang, G. P. A. Yap and C. G. Riordan, *Chem. Commun.*, 2014, **50**, 5871–5873; (b) S. K. Dey and A. Mukherjee, *New J. Chem.*, 2014, **38**, 4985–4995; (c) A. Biswas, L. K. Das, M. G. B. Drew, G. Aromí, P. Gamez and A. Ghosh, *Inorg. Chem.*, 2012, **51**, 7993–8001.
- G. Maayan and G. Christou, *Inorg. Chem.*, 2011, **50**, 7015–7021.
- (a) M. Dey, C. P. Rao, P. K. Saarenketo and K. Rissanen, *Inorg. Chem. Commun.*, 2002, **5**, 380–383; (b) M. Dey, C. P. Rao, P. K. Saarenketo, K. Rissanen, E. Kolehmainen and P. Guionneau, *Polyhedron*, 2003, **22**, 3515–3521; (c) M. Dey, C. P. Rao, P. K. Saarenketo, K. Rissanen and E. Kolehmainen, *Eur. J. Inorg. Chem.*, 2002, 2207–2215; (d) M. Dey, C. P. Rao, P. K. Saarenketo and K. Rissanen, *Inorg. Chem. Commun.*, 2002, **5**, 924–928.
- G. A. Bain and J. F. Berry, *J. Chem. Educ.*, 2008, **85**, 532–535.
- Saint, Smart and XPREP*, Siemens Analytical X-ray Instruments Inc., Madison, WI, 1995.
- G. M. Sheldrick, *SADABS Software for Empirical Absorption Correction*, University of Göttingen, Institute für Anorganische Chemie der Universität, Göttingen, Germany, 1999–2003.
- (a) G. M. Sheldrick, *SHELXS-97*, University of Göttingen, Göttingen, Germany, 1997; (b) G. M. Sheldrick, *SHELXL 97, Program for Crystal Structure Refinement*, University of Göttingen, Göttingen, Germany, 1997.
- (a) H. Miyasaka, K. Nakata, L. Lecren, C. Coulon, Y. Nakazawa, T. Fujisaki, K. Sugiura, M. Yamashita and R. Clérac, *J. Am. Chem. Soc.*, 2006, **128**, 3770–3783; (b) A. Das, K. Gieb, Y. Krupskaya, S. Demeshko, S. Dechert, R. Klingeler, V. Kataev, B. Büchner, P. Müller and F. Meyer, *J. Am. Chem. Soc.*, 2011, **133**, 3433–3443; (c) M. Hirotsu, Y. Shimizu, N. Kuwamura, R. Tanaka, I. Kinoshita,

- R. Takada, Y. Teki and H. Hashimoto, *Inorg. Chem.*, 2012, **51**, 766–768.
- 22 G. B. Deacon and R. J. Phillips, *Coord. Chem. Rev.*, 1980, **33**, 227–250.
- 23 S. Demeshko, G. Leibelng, W. Maringgele, F. Meyer, C. Mennerich, H. H. Klauss and H. Pritzkow, *Inorg. Chem.*, 2005, **44**, 519–528.
- 24 F. Arjomandirad, J. Talat-Mehrabad, N. Ziaifar and B. Shaabani, *Arch. Appl. Sci. Res.*, 2011, **3**, 480–484.
- 25 K. Nakamoto, *Infrared and Raman Spectra of Inorganic and Coordination Compounds*, Wiley, New York, 4th edn, 1986.
- 26 R. Thomas, C. B. Shoemaker and K. Eriks, *Acta Crystallogr.*, 1966, **21**, 12–20.
- 27 F. A. Cotton, E. V. Dikarev, M. A. Petrukhina and S.-E. Stiriba, *Inorg. Chem.*, 2000, **39**, 1748–1754.
- 28 E. Krickemeyer, Y. Kaiser, A. Stammler, H. Bögge and T. Glaser, *Z. Anorg. Allg. Chem.*, 2013, 1527–1533.
- 29 R. Cini, *Acta Crystallogr., Sect. C: Cryst. Struct. Commun.*, 2001, **57**, 1171–1173.
- 30 H. H. Thorp, *Inorg. Chem.*, 1992, **31**, 1585–1588.
- 31 C. Hureau, E. Anxolabéhère-Mallart, G. Blondin, E. Rivière and M. Nierlich, *Eur. J. Inorg. Chem.*, 2005, 4808–4817.
- 32 A. Prescimone, J. Wolowska, G. Rajaraman, S. Parsons, W. Wernsdorfer, M. Murugesu, G. Christou, S. Piligkos, E. J. L. McInnes and E. K. Brechin, *Dalton Trans.*, 2007, 5282–5289.
- 33 A. Yoshino, T. Miyagi, E. Asato, M. Mikuriya, Y. Sakata, K. Sugiura, K. Iwasaki and S. Hino, *Chem. Commun.*, 2000, 1475–1477.
- 34 T. C. Higgs, K. Spartalian, C. J. O'Connor, B. F. Matzkanke and C. J. Carrano, *Inorg. Chem.*, 1998, **37**, 2263–2272.
- 35 C. Mukherjee, T. Weyhermüller, K. Wieghardt and P. Chaudhuri, *Dalton Trans.*, 2006, 2169–2171.
- 36 S. Bhaduri, M. Pink and G. Christou, *Chem. Commun.*, 2002, 2352–2354.
- 37 (a) P. Kar, R. Haldar, C. J. Gómez-García and A. Ghosh, *Inorg. Chem.*, 2012, **51**, 4265–4273; (b) S. Mukherjee, K. A. Abboud, W. Wernsdorfer and G. Christou, *Inorg. Chem.*, 2013, **52**, 873–884.
- 38 M. Oh, G. B. Carpenter and D. A. Sweigart, *Chem. Commun.*, 2002, 2168–2169.
- 39 (a) R. L. Carlin, *Magnetochemistry*, Springer-Verlag, Berlin, Germany, 1986; (b) D. P. Kessissoglou, M. L. Kirk, M. S. Lah, X. Li, C. Raptopoulou, W. E. Hatfield and V. L. Pecoraro, *Inorg. Chem.*, 1992, **31**, 5424–5432.
- 40 V. Tangoulis, D. A. Malamataris, K. Soulti, V. Stergiou, C. Raptopoulou, A. Terzis, T. A. Kabanos and D. P. Kessissoglou, *Inorg. Chem.*, 1996, **35**, 4974–4983.
- 41 V. Tangoulis, D. A. Malamataris, G. A. Spyroulia, C. Raptopoulou, A. Terzis and D. P. Kessissoglou, *Inorg. Chem.*, 2000, **39**, 2621–2630.
- 42 Y. G. Li, L. Lecren, W. Wernsdorfer and R. Clérac, *Inorg. Chem. Commun.*, 2004, **7**, 1281–1284.
- 43 H. C. Yao, M. M. Li, L. M. Zheng and Z. J. Li, *J. Coord. Chem.*, 2008, **61**, 2814–2822.
- 44 S. G. Baca, I. L. Malaestean, T. D. Keene, H. Adams, M. D. Ward, J. Hauser, A. Neels and S. Decurtins, *Inorg. Chem.*, 2008, **47**, 11108–11119.
- 45 J. Mukherjee and R. Mukherjee, *Inorg. Chim. Acta*, 2002, **337**, 429–438.
- 46 (a) T. Chattopadhyay, M. Mukherjee, A. Mondal, P. Maiti, A. Banerjee, K. S. Banu, S. Bhattacharya, B. Roy, D. J. Chattopadhyay, T. K. Mondal, M. Nethaji, E. Zangrando and D. Das, *Inorg. Chem.*, 2010, **49**, 3121–3129; (b) K. S. Banu, T. Chattopadhyay, A. Banerjee, S. Bhattacharya, E. Suresh, M. Nethaji, E. Zangrando and D. Das, *Inorg. Chem.*, 2008, **47**, 7083–7093.
- 47 K. S. Banu, T. Chattopadhyay, A. Banerjee, M. Mukherjee, S. Bhattacharya, G. K. Patra, E. Zangrando and D. Das, *Dalton Trans.*, 2009, 8755–8764.
- 48 R. G. Wilkins, *Kinetics and Mechanism of Reactions of Transition Metal Complexes*, Wiley-VCH Verlag GmbH & Co. KGaA, Weinheim, Germany, 2002, p. 4.
- 49 (a) A. Jana, N. Aliaga-Alcalde, E. Ruiz and S. Mohanta, *Inorg. Chem.*, 2013, **52**, 7732–7746; (b) V. Gómez and M. Corbella, *Eur. J. Inorg. Chem.*, 2012, 3147–3155; (c) T. J. Hubin, J. M. McCormick, N. W. Alcock and D. H. Busch, *Inorg. Chem.*, 2001, **40**, 435–444; (d) M. U. Triller, D. Pursche, W.-Y. Hsieh, V. L. Pecoraro, A. Rompel and B. Krebs, *Inorg. Chem.*, 2003, **42**, 6274–6283.
- 50 (a) I. A. Koval, P. Gamez, C. Belle, K. Selmeçzi and J. Reedijk, *Chem. Soc. Rev.*, 2006, **35**, 814–840; (b) V. K. Bhardwaj, N. Aliaga-Alcalde, M. Corbella and G. Hundal, *Inorg. Chim. Acta*, 2010, **363**, 97–106.
- 51 (a) Y. Hitomi, A. Ando, H. Matsui, T. Ito, T. Tanaka, S. Ogo and T. Funabiki, *Inorg. Chem.*, 2005, **44**, 3473–3478; (b) J. A. R. Hartman, B. M. Foxman and S. R. Cooper, *J. Chem. Soc., Chem. Commun.*, 1982, 583–584; (c) A. Caneschi and A. Dei, *Angew. Chem., Int. Ed.*, 1998, **37**, 3005–3007.